PAPER • OPEN ACCESS

Early prediction of Li-ion cell failure from EIS derived from current–voltage time series

Journal of Physics: Energy

PAPER

Early prediction of Li-ion cell failure from EIS derived from current–voltage time series

M T Wilson[1,*], V Farrow[2], C J Dunn[2], L Cowie[2], M J Cree[2], J Bjerkan[3], A Stefanovska[3] and J B Scott[2]

[1] Te Aka Mãtuatua—School of Science, University of Waikato, Private Bag 3105, Hamilton 3240, New Zealand
[2] Te Kura Mata-Ao—School of Engineering, University of Waikato, Private Bag 3105, Hamilton 3240, New Zealand
[3] Department of Physics, Lancaster University, Lancaster LA1 4YB, United Kingdom
[*] Author to whom any correspondence should be addressed.

E-mail: marcus.wilson@waikato.ac.nz

Keywords: equivalent circuit model, state of health, cycle capacity, fractional integral, constant phase element, electrochemical impedance spectroscopy, wavelet analysis

OPEN ACCESS

RECEIVED
2 September 2024

REVISED
21 October 2024

ACCEPTED FOR PUBLICATION
27 November 2024

PUBLISHED
8 January 2025

Abstract

The ability to reliably detect the forthcoming failure of a rechargeable cell without removing it from its normal operating environment remains a significant goal in battery research. In this work we have cycled in the laboratory a previously-aged 3.2 A h, 3.6 V 18650 INR $LiNi_xMn_yCo_{1-x-y}O_2$ cell for 300 d until failure was apparent, using a current waveform representative of use in an electric vehicle application. Electrochemical impedance spectroscopy (EIS) down to 5 μHz was also performed on the cell as a 'gold-standard' measure, at the beginning, end and part way through the cycling. Analysis of voltage and current time series data using both parametric (equivalent circuit model) and non-parametric (wavelet-based analysis) approaches allowed us to successfully reconstruct the EIS data. As the battery aged, impedance gradually increased at frequencies between 10^{-4} Hz—10^{-1} Hz. The increase accelerated around 50 d before the battery ultimately failed. The acceleration in rate of change of impedance was detectable while the cycle efficiency remained high, indicating that a user of the cell would be unlikely to detect any change in the cell based on its performance or by common measures of state-of-health. The results imply upcoming failure may be detectable from time series analysis weeks before any noticeable drop in cell performance.

1. Introduction

The state of health (SoH) of a battery is often defined in terms of a ratio between existing charge capacity and the charge capacity when the battery is new [1]. However, there are multiple possible descriptions which emphasize various aspects of battery health, including charge or energy capacity, power delivery, and cycle efficiency [2, 3]. Such descriptors can be obtained from laboratory-based experimental measures. Possibilities include: electrochemical impedance spectroscopy (EIS) [4–7], typically measured at frequencies of ∼1Hz and higher; incremental capacity analysis (ICA) [8–11]; model-based methods that use equivalent circuit models (ECMs) or empirical models often including Kalman filters for describing battery performance and processes [12–15]; and data-driven analysis such as use of neural networks, machine learning or artificial intelligence [16–19]. A review of methodologies for SoH determination is given in Vasta *et al* [20]. Knowledge of SoH is important, especially since loss of health of a battery can manifest in many ways, depending on the failure mechanism [10, 11, 21, 22]. Markers of battery degradation include increased capacity fade, power fade and increased ohmic resistance and heat generation [11, 16, 22]. EIS is often used to demonstrate battery ageing [23–26] but can be slow and usually requires the battery to be removed from its normal operating context [20, 27], although faster implementations are available [28]. ICA allows for a detailed study of size and positions of peaks in incremental capacity $\Delta Q/\Delta V$, where Q is charge and V is voltage, as a battery ages [8–11, 29], and interpretation of such in terms of electrochemical processes.

ECMs have often been used to model batteries in terms of combinations of resistors, capacitors and constant phase elements (CPEs) [6, 12, 14, 30–34], though a wide range of different numbers of elements have been considered. For example, Westerhoff *et al* considered a model using 16 different elements each associated with a specific battery process [14], whereas Poihipi *et al* took a more phenomenological approach and reduced the Westerhoff model to just three elements [12]. Peng *et al* in a review of battery modelling methods recommended using the fewest possible circuit elements to capture necessary electrochemistry within a model [30]. Changes in different measures of SoH such as charge capacity and ohmic resistance can be related to changes in circuit parameters [33–35]. From a physical and electronic engineering perspective, there is strong motivation to use changes in circuit parameters as a method of describing and understanding battery ageing and failure. Attempts to use ECMs to capture ageing include Mauracher & Karden who have used EIS changes to describe ageing of lead-acid batteries [7], Tran *et al* who considered an ECM including state-of-charge and temperature effects to predict SoH [33], and Farrow *et al* who have used EIS and time series measurements to describe ageing of Li-ion batteries [25, 35]. Wilson *et al* used voltage and current phase differences as a measure of ageing, inferring changes from time series data [36]. However, a ECM methodology is problematic due to inherent non-linearity in batteries that cannot be captured by purely (fractional or pure) capacitive and resistive elements and limits the understanding of the problem.

Moreover, while ECMs provide a limited physical basis for interpreting EIS and battery behaviour, a key challenge is that measurements of EIS are typically done in a laboratory context, with the battery removed from its normal conditions. The ability to infer ECM parameters from real-time measurements of voltage and current would be highly valuable in industrial applications. At high frequencies ($>$0.1 Hz) a small signal containing broadband spectral information can be superposed onto the working signal [37]. However, batteries have significant energy storage at microhertz frequenices, and are often charged on a daily basis ($\sim 10^{-5}$ Hz) so other methods are required. In this work we have aimed to be able to infer EIS-like data as a battery ages from time series analysis, without the need to measure EIS itself, and thus construct understanding of ageing in terms of changes in an ECM. The goal is to be able to identify ageing in a battery *while the battery is in normal use*, without the need for it to be measured in a laboratory.

Specifically, we have taken a $LiNi_xMn_yCo_{1-x-y}O_2$ cell that has previously been used in an electric bicycle, and driven it until failure over three hundred days in the laboratory using a current waveform designed to mimic normal use using the method of Farrow *et al* [35]. Actual current supplied to the cell and simultaneous terminal voltage were recorded against time. Additionally, at the start of the experiment, part way through, and at the end, we have measured EIS with the method of Dunn [38, 39] down to frequencies of 5 μHz to provide a 'gold standard' measure as the battery ages. The 5 μHz lower frequency limit is much lower than typically used for EIS measurements—we choose to measure this low because there is significant energy storage at such frequencies and they are representative of typical use of electric vehicle batteries. We then have identified changes to the cell based on time series analysis.

In section 2 we present background theory to time series analysis. We describe our experimental methodology in section 3 and approach to analysis in terms of wavelets, ECM fitting and energy efficiency in section 4. Results are presented in section 5 and discussed in the context of battery ageing in section 6.

2. Background

There are multiple possible approaches to using time-domain data to infer plausible ECMs and their parameters [30]. One common approach is to fit a ECM to current and voltage time series directly [35, 40]: knowing the current $I(t)$ one can, for a given ECM with given parameter values, calculate the modelled voltage response $V_\mathrm{m}(t)$; a comparison of the modelled response and measured response $V(t)$ can then be undertaken for example using a least-squares based measure of goodness of fit. The circuit parameters can then be modified (e.g with the Levenberg-Marquardt algorithm [41, 42]) until the goodness of fit measure is minimized. However, modelling a voltage response to a known input current for a CPE is not straightforward since it involves fractional integrals [43–45]; numerical evaluation of these is slow and subject to subtleties in definition and interpretation. Notably there are multiple definitions of fractional integrals [46, 47] and the time history of the current is important. The handling of the history is of particular significance since practically it is not always known, making some fractional approaches more meaningful than others [48].

Wavelet analysis provides an alternative non-parametric approach to time series analysis. The continuous wavelet transformation $\tilde{x}[x(t)](s,t)$ can be defined in general terms as [49]:

$$\tilde{x}(s,t) = \frac{1}{s}\int_{u=0}^{T} \Psi^*\left(\frac{u-t}{s}\right) x(u)\,\mathrm{d}u, \tag{1}$$

where $s>0$ is a scale factor in time ($s=\omega_\psi/2\pi f$, inversely related to frequency f, where ω_ψ is a constant), $x(t)$ is a signal x defined over time t from 0 to T, and the complex-valued Ψ is a chosen wavelet. The asterisk

Table 1. A summary of the test waveforms applied to the cell in the course of the experiment. The left-hand column records the time in days since the start of the experiment; the right-hand column records the cumulative number of days of cycling.

Days since start of experiment	Description	Cumulative cycle-days at end of period
1–8	EIS 1	—
9–80	Driving	72
80	Software failure	72
84	Driving restarted	72
84–234	Driving	222
235–242	EIS 2	222
243–303	Driving	283
304–315	Driving with loss of temperature control	295
316–338	Driving	318
338	Driving terminated	318
338–345	EIS 3	318

denotes a complex conjugate. As an example of wavelet analysis, the Multiscale Oscillatory Dynamics Application (MODA) toolbox from Lancaster University github.com/luphysics/moda allows processing of time series data to infer coupling relationships between different time-varying properties [50, 51]. Specifically one can identify power and phase properties of signals at different frequency scales and identify how these change with time. For example, EIS at frequencies greater than 0.1 Hz has previously been reconstructed in this way for a hydrogen fuel cell by Du *et al* [52] and for Li-ion batteries by Hoshi *et al* [53]. We use wavelet analysis in this manuscript to construct an impedance-like spectrum from $I(t)$ and $V(t)$ measurements, which can be compared directly to EIS without the need to construct a particular ECM or evaluate the time-response of fractional elements.

In addition to reconstruction of impedance, wavelets have been used in various other ways to characterize battery behaviour. Recently, El-Dalahmeh *et al* combined wavelet transforms with neural networks to attempt to identify degradation of batteries [54]. Zhang *et al* used wavelets in order to de-noise current and voltage data taken from electric vehicles [55], and Xu *et al* considered variations in voltage wavelet amplitude from cell-to-cell as a measure of the health of a battery pack [56]. In all cases, specific ECMs were not required, making wavelet analysis a powerful tool.

Here, we apply wavelet analysis using a log-normal wavelet [57] to reconstruct the time-frequency representation of the current and voltage time series. Additionally, we apply wavelet-based phase coherence analysis [58–60] to investigate the degree of coherence between the current and voltage time-series.

3. Experimental method

3.1. Overview of method

As part of a larger investigation into battery health, we were provided with a selection of previously-aged 3.2 A h, 3.6 V 18650 INR $LiNi_xMn_yCo_{1-x-y}O_2$ cells from the electric bicycle manufacturer UBCO, ubco.co.nz. The exact history of the cells is unclear, but it is likely they were used in an electric bicycle whose battery had failed and was returned to the manufacturer. After initial tests on many of the cells, we selected a cell that appeared to be healthy in the sense that it showed normal charge and discharge behaviour.

We first measured a low-frequency EIS for the cell, using a Hewlett Packard 66332A precision current–voltage supply, and the method described in [26, 39]. We then cycled the battery at a defined current waveform for several months [35], while recording voltage and current. During this period of cycling there was a ∼4 d long interruption due to an operating system software failure. The cause of the software problem was ultimately identified and corrected, and cycling recommenced. A second EIS was measured again several months into the experiment, before further cycling occurred.

When the cell showed indications of imminent failure, as evidenced by voltage against time plots (see section 5.4 below), the driving was terminated and a third and final EIS was performed. The temperature of the laboratory was controlled to be almost always in the range 21.5 °C–22.5 °C; however there was a period between days 304 and 315 of driving over which the temperature rose to 26.5 °C and then dropped to 19.0 °C as the air-conditioning system was serviced. A summary of the testing conditions is shown in table 1.

3.2. Measuring EIS

To ensure consistency between measurements, prior to each EIS measurement the cell was discharged to 3.3 V then charged to 4.3 V, and then held at 4.06 V for several hours. EIS spectra were then measured as detailed by Dunn *et al* [26] and Dunn and Scott [39]. A frequency range of 5 μHz – 1 Hz was used. Three

cycles at the lowest frequency were applied, implying 167 h (a week) measurement time. Ideally, more cycles are required to give more reliable data, but more cycles leads to increased measurement times. Previously we have found three to be a minimum. Measuring frequencies as low as microhertz is necessary to reasonably capture the energy storage processes in an impedance spectrum [35, 36, 61].

3.3. Driving the cell

The method to drive the cell is described by Farrow *et al* [35]. A synthetic current driving profile $I_s(t)$ was produced covering 150 d in length. The profile was designed to replicate key features of the cycling of a cell while used in an electric vehicle application. The sequence consists of a period of constant current charging representing overnight charge of the cell, then a period of rest representing the vehicle not in use, an approximately hour-long sequence of rapid charge and discharge representing a morning commute with periods of acceleration and regenerative braking, a further period of rest and then another rapid charge and discharge sequence representing an evening commute. The cycling pattern is repeated but randomness is included so that the $I_s(t)$ profile is not strictly periodic.

The currents in the profile were limited between −2 A (maximum discharge rate) and 1 A (maximum charge rate). The profile $I_s(t)$ was applied to the cell using the same Hewlett Packard 66332A precision current–voltage supply as used to perform the EIS, although the supply did not always provide exactly the requested current. The cell voltage was limited to between 3.3 V and 4.3 V; when the requested current I_s was large enough to drive the voltage beyond these limits, the supply would enter constant voltage mode and reduce the charge or discharge current to keep the voltage at the limit. The voltage $V(t)$ and *actual* current supplied $I(t)$ were recorded at a mean sample rate of 8.59 Hz. An example of the current profile and the voltage of the battery is shown in figure 1.

4. Analysis

4.1. Finite-time, time-frequency analysis with logarithmic frequency resolution

We have analysed the time series data with wavelets, using the MODA toolbox produced by Lancaster University github.com/luphysics/moda [50, 51]. This analysis approach is non-parametric and does not require any model of the system. Limited analysis of the first 100 d of the sequence has been presented in [36]. We have investigated the change in a reconstructed impedance spectrum with time, as the battery ages, and compared the spectra against the EIS measurements. A normal usage current naturally contains spectral content across a wide range of time scales and can be analysed across long time windows. In order to identify a progression in cell properties, manifested through impedance spectra, with time, fourteen sections of time series data of voltage $V(t)$ and current $I(t)$ were extracted. Sections were chosen as 20 d long sequences. The 20 d sequences were selected to avoid the interrupted periods of battery cycling in an optimal way. Therefore there are small gaps between some sections. Limiting sections to twenty days in length also ensures that the data files are of manageable size without excessive downsampling.

The data for each 20 d section were pre-processed by linear interpolation to 0.01 s intervals, then applying a rolling average downsampled to 1 Hz. This resampling ensured file sizes and calculation times were kept reasonable. A wavelet transform, equation (1), was applied to both $V(t)$ and $I(t)$ sequences in each section, using a lognorm wavelet [57] with frequency resolution $f_r = 1.6$ [50, 51], to produce complex spectrograms of voltage $\tilde{V}(f,t)$ and $\tilde{I}(f,t)$. To reconstruct an impedance magnitude spectrum $Z(f)$, the power in $\tilde{V}(f,t)$ and $\tilde{I}(f,t)$ were constructed, then time averaged over the 20 d section, and finally the square-root of the ratio of the time-averages was found:

$$Z(f) = \sqrt{\frac{\left\langle \tilde{V}\tilde{V}^*(f,t)\right\rangle_{t\text{ in section}}}{\left\langle \tilde{I}\tilde{I}^*(f,t)\right\rangle_{t\text{ in section}}}}. \tag{2}$$

Averaging over power in each signal rather than amplitude places more weight on periods when the signal is strong. The phase spectrum of impedance was reconstructed as the time-average of the phase difference between $\tilde{V}(f,t)$ and $\tilde{I}(f,t)$. However, we emphasize that the reconstructed impedance spectrum is not strictly a measure of impedance which is formally defined for sine-wave current and voltage signals. The spectra for each section are compared with those measured directly by EIS.

Furthermore, we can look at the phase coherence between the voltage and current signals. Phase coherence C_θ is defined as the modulus of the average phasor between voltage and current [58–60]:

$$C_\theta = \frac{1}{\delta}\left|\int_{\tau=t-\delta/2}^{\tau=t+\delta/2} \mathrm{e}^{\mathrm{i}(\theta_V(f,\tau)-\theta_I(f,\tau))}\mathrm{d}\tau\right|, \tag{3}$$

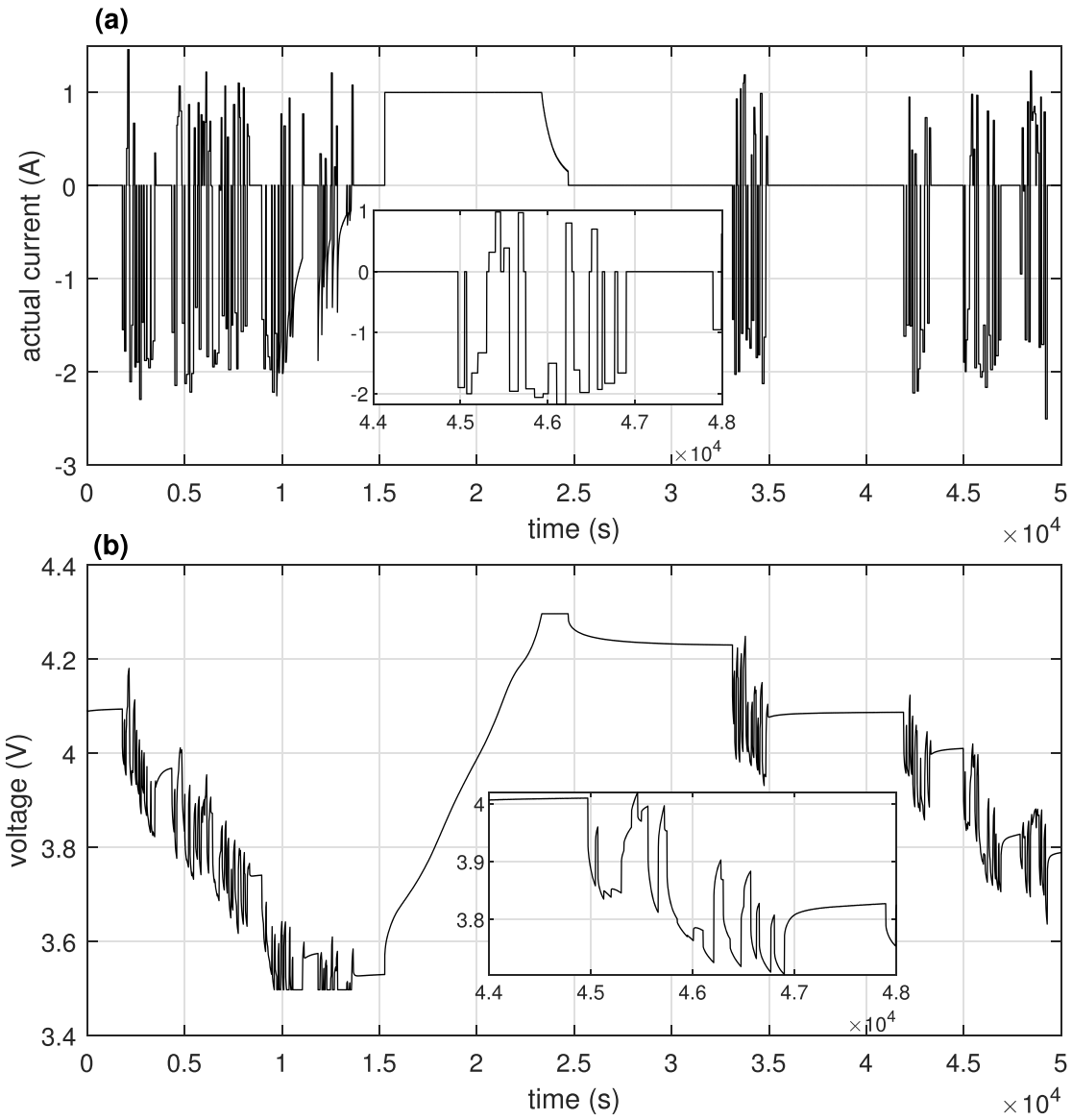

Figure 1. (a) The current applied to the cell and (b) the measured voltage of the cell for 5×10^4 s on the 223rd day of cycling. The insets show detail on a smaller timescale.

where $\theta_V(f,\tau)$ and $\theta_I(f,\tau)$ are the instantaneous phases for voltage $\tilde{V}$ and current $\tilde{I}$ spectra respectively at frequency f and time τ, and δ is a timescale for constructing averages. If there is a constant phase difference between the voltage and current phases, as would be the case for any linear ECM subject to sine wave stimuli, then $C_\theta = 1$. A reduction in C_θ denotes a variation in phase difference; ultimately $C_\theta \approx 0$ implies no correlation between the phase of the voltage and current signals. The significance of phase coherence can be tested via surrogates [62, 63]. In the analyses presented below, 140 iterative amplitude adjusted Fourier transform surrogates were used, and the coherence values shown are well above the threshold, which was defined as 95% of all surrogates.

4.2. R-CPE-CPE model

In addition to the wavelet analysis of section 4.1, we have fitted a model to the data, consisting of a resistor and two CPEs in series (R-CPE-CPE), as in figure 2. The impedance of the R-CPE-CPE circuit has been shown to give an excellent fit to measured EIS data in the frequency domain [12]. The model has also been used more recently to fit voltage responses in the time-domain [35] although fitting in the time-domain, and interpreting the result, is subtle [35, 64]. In the frequency domain, the impedance Z of the R-CPE-CPE circuit is simply the sum of the fractances of the elements:

$$Z(f) = R + \frac{1}{C_1\,(j2\pi f)^{\alpha_1}} + \frac{1}{C_1\,(j2\pi f)^{\alpha_2}}, \tag{4}$$

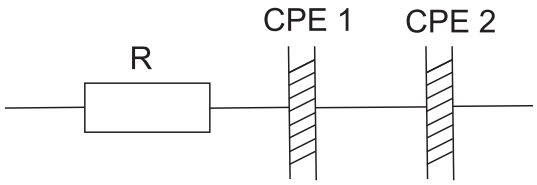

Figure 2. The equivalent circuit fitted to the time domain data; a resistor is in series with two CPEs.

where f is the frequency, R the resistance, C_1 and C_2 the fractional capacities of the two CPEs, and α_1 and α_2 the fractional orders of the two CPEs.

4.2.1. Mapping a fractance to the time domain

Interpreting a fractance equation in the time domain is, however, not straightforward. Implicitly, a frequency domain representation such as equation (4) considers the mapping between an infinitely-long sine-wave driving current and the resulting voltage response. In reality, one never has an infinitely-long history. In the time domain, for *fractional* elements, there are many possible mappings between current and voltage that result in equation (4) under driving by infinitely long sine-waves, but that produce *different* responses for driving by finite-length signal trains. Thus the question of which is the most appropriate description of a CPE in the time-domain is moot [43, 44].

In this work, we follow Hartley *et al* [65] and choose to define the fractional integral of order α of the current $I(t)$ by the Riemann–Liouville integral [45, 46, 66] starting at time equals zero:

$$u^{\alpha}\left[I(t)\right](t) = \frac{1}{\Gamma(\alpha)}\int_{t'=0}^{t}(t-t')^{\alpha-1}I(t')\,\mathrm{d}t'. \tag{5}$$

Equation (5) indeed returns the required amplitude and phase when subjected to an infinitely-long sine-wave driving [64] but we recognize it is only one possibility of many. The main advantages of the choice are that it has an intuitive interpretation in terms of a Green function, and it provides a straightforward calculation of the fractional integral although it does not necessarily lead to the most accurate representation of the battery in practice. For example, an alternative formulation considers a cell as more accurately described by a time-changing capacitance [64, 67]. A final point with the chosen definition is that $u^{\alpha}(t=0)$, as given by equation (5), is zero. The formulation takes no account of history beyond the start of a series of data. To account for existing charge within the battery at the start of a time sequence, we need also to add an ideal voltage source (that is, a constant voltage V_{c}) into the R-CPE-CPE circuit. Clearly this adjustment is physically incorrect, but results show that the choice is not significant for the purposes of ECM modelling and SoH evaluation.

4.2.2. Linear optimization

Since a model consisting of series elements produces a voltage given by the sum of the voltages across each element, it is straightforward to optimize the component values for a R-CPE-CPE circuit, R, C_1, C_2 and V_{c}, using least-squares optimization.

Specifically, assuming α_1 and α_2 are known, we can write:

$$V_{\mathrm{m}}(t) = V_{\mathrm{c}} + RI(t) + \left[\frac{1}{C_1}\right]u_1(t) + \left[\frac{1}{C_2}\right]u_2(t), \tag{6}$$

where $V_{\mathrm{m}}(t)$ is the modelled response to the input current $I(t)$. Here,

$$u_1(t) = \frac{1}{\Gamma(\alpha_1)}\int_{t'=0}^{t}(t-t')^{\alpha_1-1}I(t')\,\mathrm{d}t', \tag{7}$$

and similarly for $u_2(t)$ with α_2. For a given current $I(t)$ and orders α_1 and α_2, equation (6) is the sum of known functions of time, each multiplied by a constant. Thus one can use least-squares optimization to find the values of V_{c}, R, $1/C_1$ and $1/C_2$ that minimize

$$\tilde{S}^2\left(V_{\mathrm{c}}, R, 1/C_1, 1/C_2; \alpha_1, \alpha_2\right) = \Sigma_t\left[V_{mt} - V_t\right]^2, \tag{8}$$

for a given α_1 and α_2 where $V_{\mathrm{m}t}$ and V_t are the modelled and measured voltages respectively as a function of discrete time t. The minimum value of $\tilde{S}^2$ over V_{c}, R, $1/C_1$ and $1/C_2$ for a given α_1 and α_2 is denoted by $S^2(\alpha_1, \alpha_2)$.

This optimization is extremely fast, but the method requires knowledge of $u_1(t)$ and $u_2(t)$, which depend on choices of α_1 and α_2 respectively. To implement the optimization, we therefore first calculate $u_1(t)$ and $u_2(t)$ for a range of different α_1 and α_2 values using the numerical calculation detailed below in section 4.2.3, and then optimize the remaining parameters for each possible combination pair of α_1 and α_2. Overall, one of the pairs will result in the lowest value of $S^2(\alpha_1, \alpha_2)$, which defines the optimum α_1 and α_2, along with V_c, R, $1/C_1$ and $1/C_2$. Specifically, in this work, we considered values of α_1 from 0.92 to 1.00 in steps of 0.005; and values of α_2 from 0.05 to 0.60 in steps of 0.01. These ranges covered almost all the cases considered.

While the method is quick, it relies on the linear superposition of circuit-element voltages, which is only applicable when a series circuit is used.

4.2.3. Calculation of fractional integrals

Numerically, we need to calculate equation (5) in discrete time, since data is recorded only at discrete time intervals. A numerical problem arises with equation (5) in that $(t-t')^{\alpha-1}$ diverges as $t' \to t$. This can be alleviated by integrating equation (5) by parts. Writing $x = I(t')$ and $\mathrm{d}y = (t-t')^{\alpha-1}\mathrm{d}t'$, and using the identity

$$\int_a^b x\,\mathrm{d}y = [xy]_a^b - \int_a^b y\,\mathrm{d}x, \tag{9}$$

we obtain:

$$u^{\alpha}\left[I(t)\right](t) = \frac{1}{\alpha\Gamma(\alpha)}\left(I(t=0)\ t^{\alpha} + \int_{t'=0}^{t}(t-t')^{\alpha}\,\mathrm{d}I(t')\right). \tag{10}$$

Equation (10) can now be naturally discretized as:

$$u_N^{\alpha} = \frac{1}{\alpha\Gamma(\alpha)}\left[I_0 t_N^{\alpha} + \sum_{i=1}^{N-1}(t_N - t_i)^{\alpha}\,\Delta I_i\right] \tag{11}$$

where u_N^{α} is the fractional integral to time t_N, I_0 is the initial current and $\Delta I_i = I_i - I_{i-1}$ denotes the change in current between the $(i-1)$th and ith time points. The formalism of equation (11) removes the singularity when $t' = t$ and additionally does not require time steps to be exactly equal.

4.3. Energy-efficiency description

We also evaluate the cycling efficiency as the cell ages, using the method of Dunn [38]. Since the driving wave is not periodic, the cycle efficiency requires careful definition. We define a pseudo-cycle as the period over which a cell returns to a V and Q state that is sufficiently close to a previous V and Q state. In other words, we construct the trajectory of the cell in a phase-space defined by $V(t)$ and $Q(t) = \int_{t'=0}^{t} I(t')\mathrm{d}t'$ and look for times t_f (f denoting 'finish') and t_s (s denoting 'start') such that $V(t_f) = V(t_s)$ and $Q(t_f) = Q(t_s)$ to some defined tolerance. There are many such pseudo-cycles, some of which can be overlapping.

Over each pseudo-cycle t_s to t_f we evaluate efficiency U, defined as:

$$U = \frac{U_-}{U_+}, \tag{12}$$

where

$$U_- = -\int_{t'=t_s}^{t_f}\left[V(t')I(t')\right]_-\mathrm{d}t' \tag{13}$$

and

$$U_+ = \int_{t'=t_s}^{t_f}\left[V(t')I(t')\right]_+\mathrm{d}t'. \tag{14}$$

In equation (13) the integral is evaluated over those times between t_s and t_f where the power VI is negative, i.e. when energy is extracted from the battery, thus U_- is a positive quantity, and in equation (14) the integral is evaluated over those times where the power is positive, i.e. when energy is supplied to the battery.

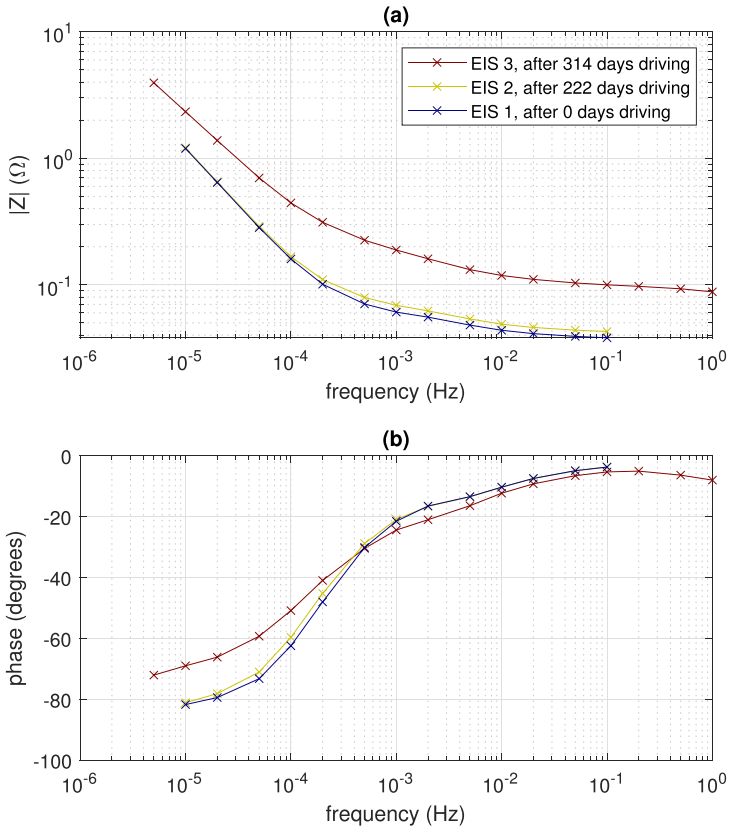

Figure 3. (a) The magnitude and (b) the phase of the EIS of the cell measured with the method of Dunn and Scott [39], at the beginning of the experiment (dark blue line), after 222 d of cycling (dark yellow line) and after 314 d of cycling (dark red line). The colours are consistent with the progression of sequences shown in figure 4 below.

5. Results

5.1. Progression of EIS

Figure 3 shows (a) the magnitude and (b) the phase of the impedance as measured with EIS using the method of Dunn and Scott [39]. The three impedance measurements were made at the start of the experiment (dark blue), after 222 d of driving (dark yellow) and after 314 d of driving (dark red), as summarized in table 1. The EIS spectrum shows a near capacitive impedance at frequencies lower than around 10^{-4} Hz, but transitioning to low-order fractional behaviour (near resistive) at frequencies higher than around 10^{-2} Hz. There is a small increase in magnitude of impedance at higher frequencies between the start of the experiment and 222 d of driving, but after 314 d the impedance has increased significantly over all frequencies measured.

5.2. Finite-time, time-frequency analysis with logarithmic frequency resolution

Figure 4 shows the impedance in the 20 d segments as constructed by the non-parametric wavelet analysis of time series data by the MODA toolbox. The chronological progression in the lines is from blue to red. Part (a) shows the magnitude of the impedance against frequency for ranges 5×10^{-5}–2×10^{-2} Hz. Part (b) shows the phase difference between voltage and current for the same frequency range. At the lowest frequencies ($<5 \times 10^{-5}$ Hz) the constructed impedance has a high error due to only a few cycles being present in the data and is not shown. The first EIS measurement is also shown by the dark blue stars for comparison. Results are broadly consistent with those obtained experimentally with EIS in the frequency domain, figure 3. There, a near capacitive impedance at frequencies lower that 10^{-4} Hz transitions towards a low fractional order capacitance at higher frequencies. However, comparing the MODA toolbox day 1–20 sequence (darkest blue line) with the first EIS measurements (dark blue stars) it is clear that the MODA toolbox results show a higher impedance than the EIS results in the range 2×10^{-4}–5×10^{-3} Hz. Additionally, there is a small peak in impedance as reconstructed by the MODA toolbox in the frequency region around 4×10^{-4} Hz and 5×10^{-4} Hz. Its origin is unclear, and needs further investigation. The peak is marked by a dashed line on figure 4.

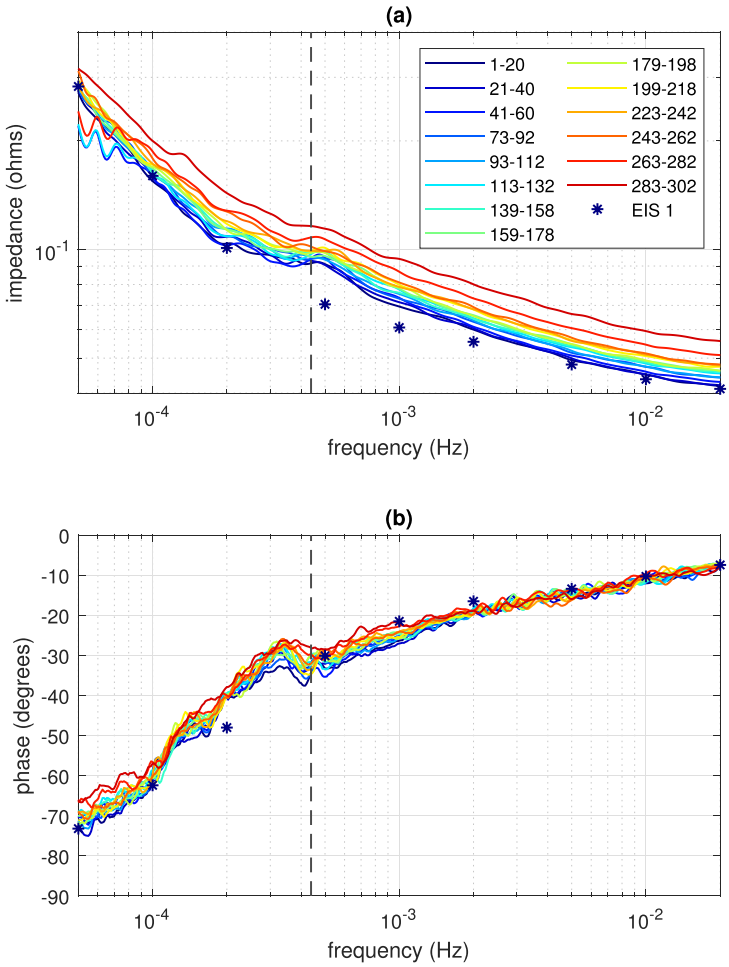

Figure 4. (a) The magnitude, and (b) the phase of the recovered impedance spectrum $Z(f)$ from 5×10^{-5} Hz to 2×10^{-2} Hz derived from wavelet amplitude and phase obtained by the lognormal wavelet using the MODA toolbox [50, 51, 57], for fourteen 20 d periods through the course of the experiment. The caption indicates the day ranges of cycling for each section, blue the earliest, red the latest. The initial EIS measurement of figure 3 is shown with the dark blue stars. The magnitude plot (a) shows a progression upward in impedance magnitude, particularly at lower frequencies, that accelerates as the battery ages. The dashed line marks the frequency 4.39×10^{-4} Hz.

Figure 5 shows the phase coherence (equation (3)) between the current and voltage wavelet transforms $\tilde{I}(f,t)$ and $\tilde{V}(f,t)$ respectively, for the same fourteen 20 d sections, progressing blue to red chronologically. As expected, due to a small number of cycles used to calculate the coherence, the phase coherence is nearly unity at the lower frequencies [62]. However, phase coherence reduces for the higher frequencies, possibly indicating an increased level of noise or non-linearity at the higher frequencies. Notably, there is a 20% drop in phase coherence at around 3×10^{-4}–5×10^{-4} Hz; this drop aligns with the small peak in impedance seen on figure 4(a) at the same frequency. Its position is marked by the dashed line on figures 4 and 5. As the battery ages, this drop disappears. When 20 d are taken into account, the number of cycles at the very low frequency end ($<5 \times 10^{-5}$ Hz) is insufficient to reliably calculate the phase coherence [58, 62]. Moreover, the phase difference is highly variable indicating that the obtained values of phase coherence are not reliable and thus they are not shown.

5.3. Fit to R-CPE-CPE

Figures 6 and 7 show with the black crosses the magnitude and phase respectively of the impedance for each day at six frequencies, as calculated using fits to the R-CPE-CPE model. That is, for each day we have fitted α_1, α_2, C_1, C_2 and R, and calculated the impedance with equation (4). The fits to each day are shown with the black crosses. The impedance magnitude at all frequencies rises as the battery ages, but the trend shows most clearly with frequencies 10^{-4} Hz, panel (b), and 10^{-3} Hz, panel (c), where day-to-day fluctuation in impedance magnitude is lowest. Notably, one can observe an acceleration upward in impedance magnitude after around 280 d. The fitted impedance values (black crosses) generally agree well with the three EIS measurements (red stars). For frequencies 10^{-1} Hz and lower, the third EIS measurement (EIS 3) is higher than the daily impedance fits. At this time the cell was degrading quickly with use, and it is likely that its

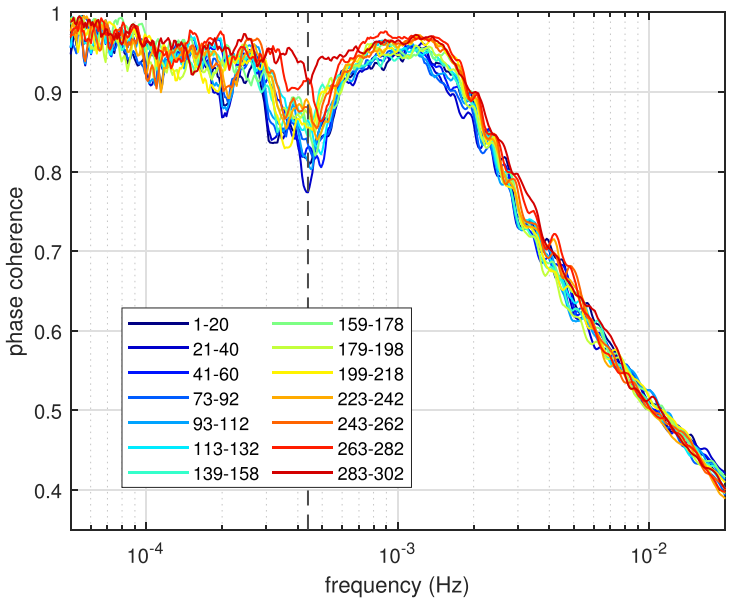

Figure 5. The phase coherence between current and voltage for frequencies between 5×10^{-5} and 2×10^{-2} Hz, for the fourteen different 20 d sequences as shown in the legend, blue the earliest and red the latest. The dashed line marks the frequency 4.39×10^{-4} Hz.

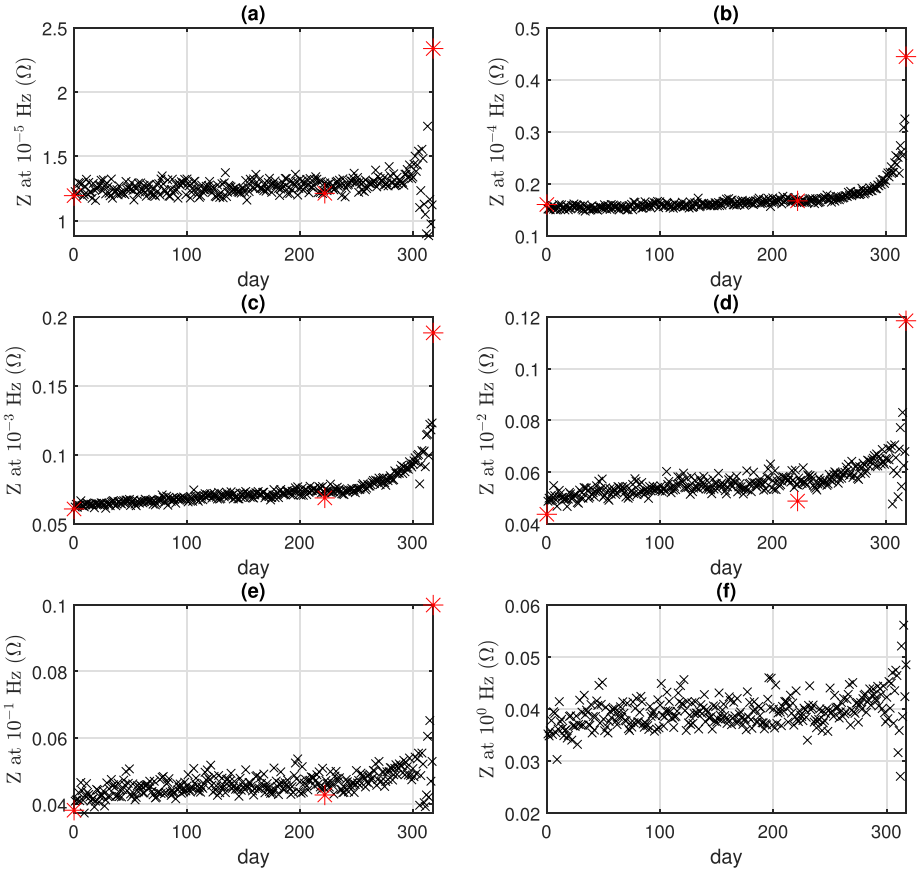

Figure 6. The magnitude of impedance (i) as fitted by the R-CPE-CPE equivalent circuit model calculated for each day (black crosses), and (ii) as measured by EIS (red stars). Six frequencies are selected for the fits to R-CPE-CPE: (a) 10^{-5} Hz, (b) 10^{-4} Hz, (c) 10^{-3} Hz, (d) 10^{-2} Hz, (e) 10^{-1} Hz and (f) 10^{0} Hz.

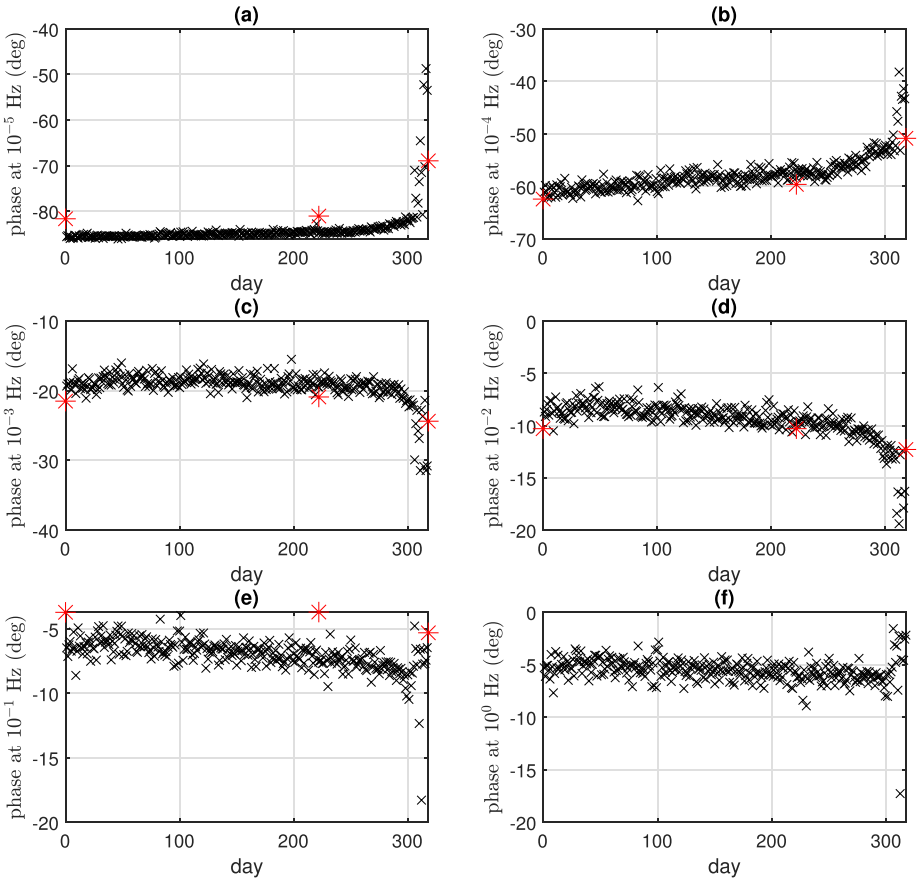

Figure 7. The phase of impedance (i) as fitted by the R-CPE-CPE equivalent circuit model calculated for each day (black crosses), and (ii) as measured by EIS (red stars). Six frequencies are selected for the fits to R-CPE-CPE: (a) 10^{-5} Hz, (b) 10^{-4} Hz, (c) 10^{-3} Hz, (d) 10^{-2} Hz, (e) 10^{-1} Hz and (f) 10^{0} Hz.

impedance rose significantly during the course of the EIS measurement, making the interpretation of the EIS 3 measurement more uncertain than for EIS 1 and EIS 2.

The movement of the fitted phase with ageing depends on frequency is shown by the black crosses in figure 7; at the lowest frequencies the phase becomes less negative with ageing whereas the phase becomes more negative at the highest frequencies. The fitted phase values (black crosses) agree well with the EIS measurements (red stars), particularly at frequencies of 10^{-4} Hz and 10^{-5} Hz.

We also show in figure 8 the fitted parameter values for the R-CPE-CPE model. Notably, in part (a), we see the fitting of the highest order CPE is remarkably constant with time, with α_1 fitted almost always as 1.00, implying a pure capacitor. Broadly, in part (c) we see α_2 rises with time (the order of the second CPE increases; it becomes less like a resistor), and in part (e) we observe a slow increase in resistance with ageing, that accelerates rapidly at around day 300 of cycling. There is considerable variation in α_2, C_2 and R from day to day, implying that the fitting method often struggles to separate the lowest order CPE from the resistor. However, while there is a wide variation in the parameter values, the magnitude of $Z(f)$, figure 6, remains much more steady with changing day.

Figure 9 shows (a), (b) current and (c) and (d) actual (thick grey) and fitted (thin black) voltage for day 223 of driving, as an example of the quality of fit in the time domain. The plots (b) and (d) show the same data as (a) and (c) respectively, but over a shorter time period to clarify the detail. The charging periods are fitted well; however there are some periods such as the rest period after charging where the fit is ∼20 mV in discrepancy. In figure 10 we show the landscape of $S(\alpha_1, \alpha_2)$, as defined in equation (8), for day 223 of driving. The value of α_1 is tightly constrained to be close to 1; whereas α_2 is much more loosely specified. The wide range of plausible α_2 values leads to the spread of data seen in figure 8(c).

5.4. Failure mode

In the days before the experiment was terminated, there were occasions when the cell showed negative differential capacitance. That is, a positive, charging current resulted in a decrease in voltage. These negative differential capacitance occurrences commenced during day 312 of cycling and were daily or twice daily

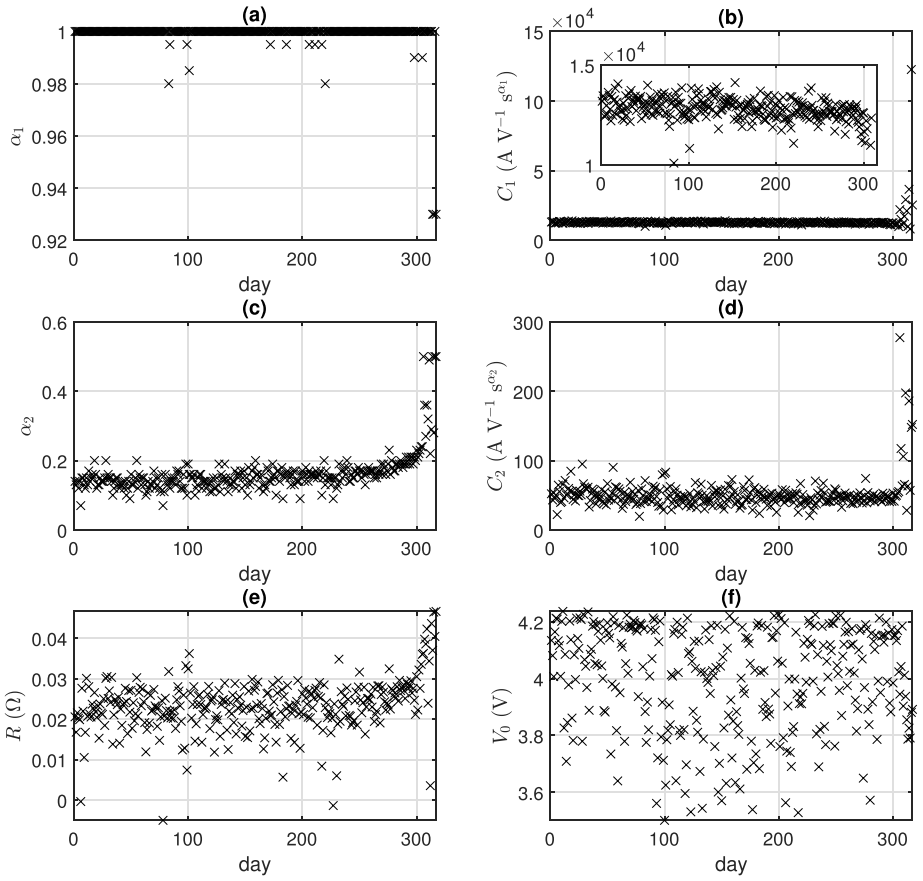

Figure 8. The fitted parameters (a) α_1, (b) C_1 (the inset is the same data on a finer scale), (c) α_2, (d) C_2, (e) R and (f) V_0 for each day.

events from then until the cycling was stopped. Figure 11 shows (a) $I(t)$ and (b) $V(t)$ for the final day for which data were recorded. During this period there are two such occurrences, shown by the pairs of blue dashed lines. The data are suggestive of an intermittent leak path occurring as the cell ages, and consistent with lithium plating as a possible ultimate failure mechanism [11, 68].

5.5. Cycle efficiency

Figure 12 shows the cycle efficiency as a function of time as the cell ages. Note that for the large majority of the sequence, U remains close to one, indicating a highly-efficient cell. Although a trend downwards in U is evident even as early as 20 d (∼500 h) into the experiment, it is a very gradual decline in efficiency, from approximately 0.955 to 0.945 after around 250 d (6000 h). This decline would unlikely be noticed by a user. At around 250 d the U parameter begins to decline more rapidly, dropping to ≈0.935 in the next 40 d (∼1000 h). At around 310 d of cycling, the pseudo-cycle method fails as the system fails to return to a previous point in V-Q-space.

Overall, the cycle efficiency, as defined over pseudo-cycles, denotes a single-valued measure of the health of the cell, based on time series data of voltage and current collected while the cell is in normal operation.

6. Discussion

Cycling a cell for almost a year has provided valuable data in multiple regards. Notably, we have demonstrated that we can recover EIS-like data from time series of voltage and current from when the cell is being 'normally' cycled, indicating the possibility of detecting upcoming failure without having to undertake specific laboratory tests such as EIS or ICA. Production of an EIS-like spectrum can be achieved either through a non-parametric wavelet analysis or through fitting of an ECM. Moreover, for the specific cell tested, we show that it is possible to detect the upcoming failure a few weeks before any loss in performance would become evident to a user of the battery.

First, we have reproduced the 'gold standard' EIS measurements of figure 3 using wavelet analysis of $V(t)$ and $I(t)$ through the MODA toolbox. Notably, the impedance spectra obtained by time-frequency analysis

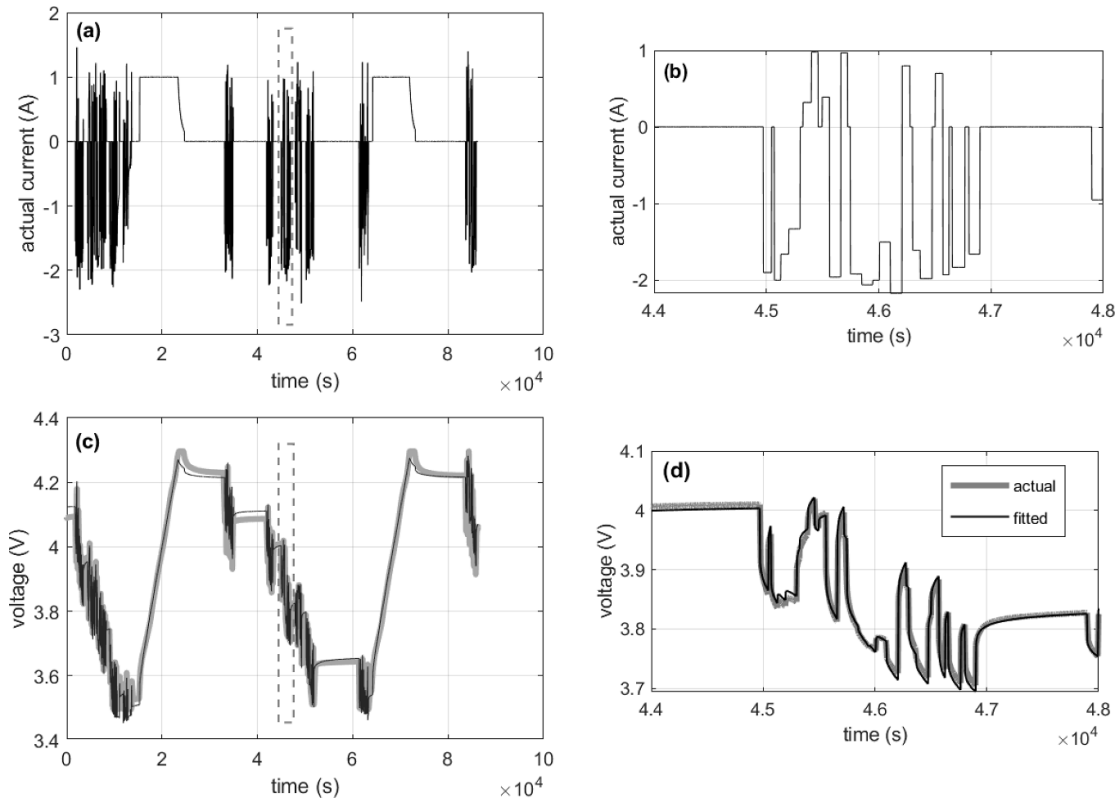

Figure 9. (a) A plot of current against time for Day 223 of driving. (b) An enlarged version of (a) over a shorter time interval as indicated by the dashed box in (a). (c) A plot of measured (thick grey) and fitted (thin black) voltage over the same period. (d) An enlarged version of (c) over the same time-interval as (b) to show further detail.

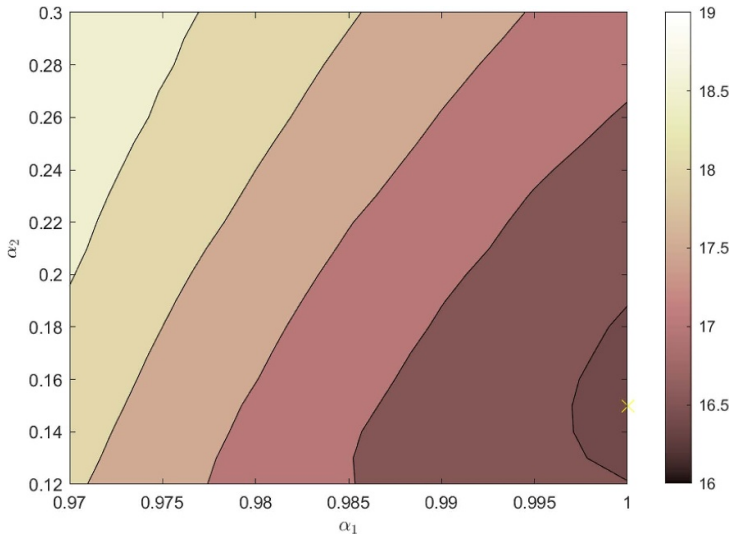

Figure 10. A plot of $S(\alpha_1, \alpha_2)$ as defined in equation (8) for Day 223 of driving as a function of α_1 and α_2, the orders of the CPEs in the R-CPE-CPE model. The colour scale is in millivolts. The minimum is at $\alpha_1 = 1.00$ and $\alpha_2 = 0.15$. The value of α_1 is tightly defined, but there is a wider range of plausible α_2 values.

with logarithmic frequency resolution using the MODA toolbox, shown in figure 4, are in broad agreement with the EIS results. They show similarly-shaped spectra; specifically at low frequencies ($<10^{-4}$ Hz) there is capacitative behaviour and there is little change in impedance magnitude up to 263 d of cycling, whereas at higher frequencies ($>10^{-2}$ Hz), the impedance spectrum is more resistive, and there is a small increase in magnitude with ageing. After 263 d the impedance magnitude rapidly increases across all frequencies. The change in impedance can be attributed to a growth in the amplitude of the voltage signal $\tilde{V}(f, t)$ with time. Time-frequency analysis using the MODA toolbox shows however a higher reconstructed impedance

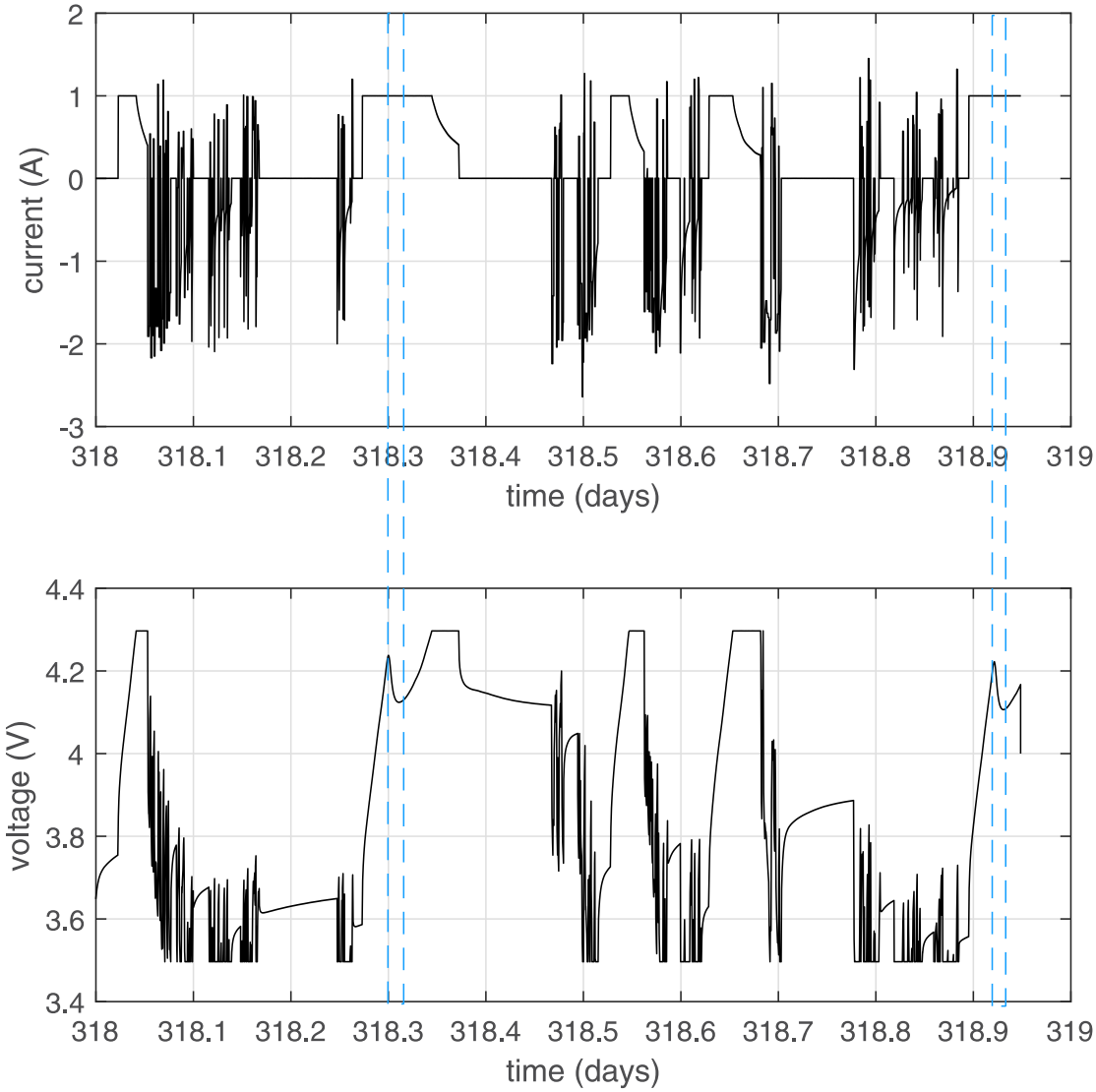

Figure 11. The failure of the cell as evidenced in the time domain. (a) The current and (b) the voltage against time. In the two regions indicated by the pairs of blue dashed lines, a positive, charging current results in a reduction in voltage.

than EIS measurements around 2×10^{-4}–5×10^{-3} Hz. They also show notable features at around 3×10^{-4}–5×10^{-4} Hz: a small peak in impedance magnitude seen at the marked frequency in figure 4(a), a kink in the phase as seen in figure 4(b), and a drop in phase coherence seen in figure 5. The reasons for these features are unclear, but it is noteworthy that they disappear as the battery ages and are possibly due to chemical effects in the cell or biases in the synthetic current waveform. The small rise in impedance at this frequency range is not seen in the EIS spectra in figure 3; however, the EIS spectra were taken over a coarse frequency resolution of 3 points per decade. To fully understand the physics of battery ageing, the origin of the frequency effects needs investigation. It might be possible to link the frequency and amplitude of time-frequency features to chemical processes, for example. We note that as the battery ages it spends a larger fraction of time at its upper and lower voltage limits, influencing oscillatory characteristics.

Second, we have compared a time progression in impedance across specific frequency bands with the fits of a fractional equivalent circuit model, as described in section 4.2. Figures 6 and 7 show the magnitude of the fitted impedance and its phase respectively, by the black crosses, for each day of cycling, at different frequencies. The plots are in broad agreement with EIS data (red stars) across all frequencies, though agreement is best between 10^{-4} Hz and 10^{-2} Hz, and with the time-frequency using the MODA toolbox. Fitting a ECM also generates insight into how the cell's electronic properties might be changing via variation in circuit parameters, as shown in figure 8. Notably for this particular cell there is an increase in the order of the second CPE α_2, denoting that this fractional impedance is becoming more capacitive and less resistive. The impedance of the second CPE is most significant compared to the first CPE and the resistor in the frequency range 0.1–10 mHz; below this range the first CPE dominates, above this range the resistor

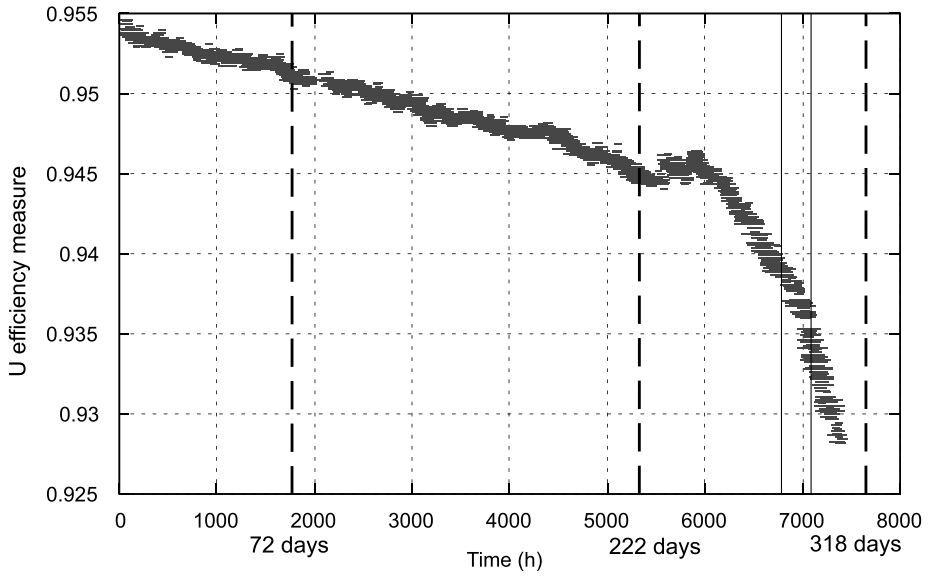

Figure 12. The cycle efficiency U, as defined by equation (12), evaluated over pseudo-cycles, as the cell ages. The left-hand and right-hand extent of the bars denote the start time t_s and the finish time t_f of each pseudo-cycle respectively. The dashed lines are positioned where cycling was interrupted to perform the EIS measurements at 72 d, 222 d and 318 d of cycling; the solid vertical lines denote the period for which tight temperature control on the laboratory was lost (see table 1). The algorithm to find pseudocycles fails just before the end of the experiment.

dominates. This second CPE is often associated in the literature with diffusive processes [6, 14] and it is plausible that changes in impedance in this range are related to changes in diffusion of ions across the separator. There is also a rapid increase in resistance from day 300 onwards, consistent with loss of lithium inventory or surface-electrolyte interface growth [11]. We note that applying a fractional model in the time domain is challenging, due to multiple possible formulations of fractional integrals in the time domain [43, 64, 66]. While there are advantages and disadvantages to the various possibilities, we have chosen the formulation of equation (11) since it provides simplicity in computation. However, a notable disadvantage is that it fails to consider the immediate history to a sequence, which is of importance in fractional systems [43]. These disadvantages notwithstanding, results demonstrate that meaningful ECM parameters can be identified. Additionally, the ability to fit circuit parameters quickly relies on the elements being in series (and thus all having the same current $I(t)$). While the R-CPE-CPE series model is adequate in many cases [12] it will not be appropriate for all cells, for example $LiFePO_4$ which have a component parallel to the lowest order CPE evident at low frequency. Other schemes for fitting an ECM will be required for non-series models where one does not have the same current through each element, such as using a SPICE-based model of a CPE [69]. While the inclusion of a CPE in the ECM has been made on the basis of fitting of ECMs to experimental data [12], and tested through the time-domain fitting in this manuscript, further confirmation of its presence could be obtained from hysteresis curves. A CPE would show hysteresis—that is, the charge versus voltage plots for charge and discharge would not align—even in the limit of vanishingly small currents [36, 70]. This is in contrast to what would happen with a ECM consisting of only capacitative and resistive elements, for which hysteresis would reduce to zero in the limit of zero current.

Third, in figure 12, we show the change in cycle efficiency as the cell ages. It is important to note that the cell has not been cycled in any consistent test cycle, but has been charged and discharged in a manner representative of use in an electric vehicle. We have constructed efficiency by identifying points in time where the battery returns to a similar charge and voltage state as a previous point in time, and evaluated the energy into the cell during charge and energy out of the cell during discharge over these 'pseudocycles'. The ratio of the energy out to the energy in gives a measure of efficiency U, as in equation (12). The measure is highly consistent, and its slow reduction with cell ageing is easily discerned over just a few days of cycling. At around 250 d (6000 h) of driving, figure 12 shows that the rate of decline of battery efficiency has increased, suggestive of upcoming failure. At around 290 d (approximately 7000 h) the rate of decline of U increases further. The rapid decline in U is similar to what is often seen in the traditional SoH measure of charge capacity [16]. While the rates of decline are clearly discernable, the actual drop in U is small (from 0.955 to 0.935 across about 290 d of driving) it would still be unlikely that a user would detect any loss of performance until close to day 318, where the experiment was terminated and the final EIS measured. The

implication is that time-frequency analysis of the time series data provides warning that a failure is occurring, a few weeks before the failure would become apparent to a user.

Fourth, we emphasize there are conceptual difficulties regarding interpretation of impedance data. Strictly, impedance is defined for infinitely long sine wave current and voltage signals for static systems. Fourier-based analysis of experimental data requires windowing, which necessarily introduces biases into spectral data depending on window length. In our cycling experiment the current and voltage signals are far from harmonic; while wavelet analysis can produce $\tilde{I}(f,t)$ and $\tilde{V}(f,t)$, identifying the ratio of $\tilde{V}$ to $\tilde{I}$ in some form as an impedance is debatable. Nevertheless, the similarity between $\tilde{Z}(f,t)$ averaged over 20 d sections, figure 4, and EIS measurements, figure 3, offers some empirical validity. Additionally, the properties of the cell clearly change with time but we analyse data in defined time sections assuming the properties are locally static within each section. Any Fourier-based analysis implicitly assuming long (psuedo-infinite) time sequences is problematic. Most evidently, figure 6 shows a rapid change in cell properties after 300 d of cycling and analysis in this time period requires careful interpretation. Notably, the third EIS measurement does not align well with the daily fitted impedance values. The EIS measurement takes approximately two weeks to make, and given the cell's advanced state of failure it is likely that its impedance has changed significantly during the course of the EIS 3 measurement, leading to considerable experimental uncertainty.

Finally, we note there are shortcomings with the experiment. In particular, we report data from a single $LiNi_xMn_yCo_{1-x-y}O_2$ cell, whose history before the experiment is not completely clear. While we have demonstrated that we can use time series analysis of $I(t)$ and $V(t)$ data in approximately normal operating conditions to demonstrate degradation of this particular cell, it may not be possible to do so in all cases. Additionally, we note that problems were experienced because of the length of time of the experiment. Notably a software failure caused a break in the driving of the cell after 72 d of cycling, and the tight temperature control of the laboratory was lost over about 12 d towards the end of the experiment. The loss of temperature control occurred during the time where cell degradation appeared to be accelerating, and possibly though not necessarily contributes to the rapid decline in cell health [13]. Furthermore, the cell was driven with a current $I(t)$ that was constructed to be broadly representative of the cell in its intended application in an electric bicycle. However, the constructed current, using the method described by Farrow *et al* [35], produces a profile that shows sharper changes in current than likely in practice. These sharp transitions might influence degradation mechanisms or influence the success of the wavelet and ECM-fitting algorithms compared to the case of real current and time data obtained from actual use. Additionally, while we measured EIS as a 'standard' basis by which to assess our time series analyses, we did not measure charge capacity, a traditional method in which SoH is tracked in the laboratory.

7. Conclusion

In this work we have cycled a $LiNi_xMn_yCo_{1-x-y}O_2$ cell in the laboratory for approximately a year, until it has failed. For this cell, failure was evident in the time domain by the cell being unable to hold a voltage. Most clearly this can be seen in figure 11 which shows periods where a positive *charging* current results in a *reduction* in voltage. Further research is needed to identify the exact processes occuring in these negative differential capacity events. In the frequency domain, as evidenced by EIS and reconstructed impedance spectra from the time domain, the failure manifested as a rapid rise in impedance at around 10^{-4}–10^{-3} Hz. This frequency corresponds to a timescale of ∼20 min to ∼3 h, notably longer than timescales used in previous work for EIS [4, 5], and demonstrates the value in taking EIS to very low frequencies. The transition to failure could be detected from time-domain measurements of normal cycling at around 40 d before failure occurred using (i) wavelet analysis, (ii) fitting of a R-CPE-CPE equivalent circuit, and (iii) evaluation of cycle efficiency. The early detection of failure for this one cell suggests that the methods of time-frequency analysis described in this paper may be of significant value in anticipating battery failure more broadly.

Data availability statement

The raw voltage and current time series data are available on request to the corresponding author. The MODA toolbox for time series analysis is available at github.com/luphysics/moda [71]. The MATLAB code for fitting the ECM is available at https://github.com/mtwilson1970/Fractional_ECM_fitting [72].

ORCID iDs

M T Wilson https://orcid.org/0000-0001-6214-7727
A Stefanovska https://orcid.org/0000-0001-6952-8370

References

[1] Pop V, Henk J B, Danilov D, Regtien P P L and Notten P H L 2008 *Battery Management Systems: Accurate State-of-Charge Indication for Battery-Powered Applications* (Springer)
[2] Huotari M, Arora S, Malhi A and Främling K 2021 Comparing seven methods for state-of-health time series prediction for the lithium-ion battery packs of forklifts *Appl. Soft Comput.* **111** 107670
[3] Ungurean L, Cârstoiu G, Micea M V and Groza V 2017 Battery state of health estimation: a structured review of models, methods and commercial devices *Int. J. Energy Res.* **41** 151–81
[4] Messing M, Shoa T and Habibi S 2021 Estimating battery state of health using electrochemical impedance spectroscopy and the relaxation effect *J. Energy Storage* **43** 103210
[5] Zappen H, Fuchs G, Gitis A and Uwe Sauer D 2020 In-operando impedance spectroscopy and ultrasonic measurements during high-temperature abuse experiments on lithium-ion batteries *Batteries* **6** 25
[6] Berthier F, Diard J-P and Michel R 2001 Distinguishability of equivalent circuits containing CPEs: part I. Theoretical part *J. Electroanal. Chem.* **510** 1–11
[7] Mauracher P and Karden E 1997 Dynamic modelling of lead/acid batteries using impedance spectroscopy for parameter identification *J. Power Sources* **67** 69–84
[8] Jenu S, Hentunen A, Haavisto J and Pihlatie M 2022 State of health estimation of cycle aged large format lithium-ion cells based on partial charging *J. Energy Storage* **46** 103855
[9] Schaltz E, Stroe D-I, Nørregaard K, Ingvardsen L S and Christensen A 2021 Incremental capacity analysis applied on electric vehicles for battery state-of-health estimation *IEEE Trans. Ind. Appl.* **57** 1810–7
[10] Osara J A, Ezekoye O A, Marr K C and Bryant M D 2021 A methodology for analyzing aging and performance of lithium-ion batteries: consistent cycling application *J. Energy Storage* **42** 103119
[11] Anseán D, Manuel García V, González M, Blanco-Viejo C, Carlos Viera J, Fernández Pulido Y and Sánchez L 2019 Lithium-ion battery degradation indicators via incremental capacity analysis *IEEE Trans. Ind. Appl.* **55** 2992–3002
[12] Poihipi E, Scott J and Dunn C 2022 Distinguishability of battery equivalent-circuit models containing CPEs: updating the work of Berthier, Diard, & Michel *J. Electroanal. Chem.* **911** 116201
[13] Imran R M, Li Q and Flaih F M F 2020 An enhanced lithium-ion battery model for estimating the state of charge and degraded capacity using an optimized extended Kalman filter *IEEE Access* **8** 208322–36
[14] Westerhoff U, Kurbach K, Lienesch F and Kurrat M 2016 Analysis of lithium-ion battery models based on electrochemical impedance spectroscopy *Energy Technol.* **4** 1620–30
[15] Pannala S, Turner J A, Allu S, Elwasif W R, Kalnaus S, Simunovic S, Kumar A, Jay Billings J, Wang H and Nanda J 2015 Multiscale modeling and characterization for performance and safety of lithium-ion batteries *J. Appl. Phys.* **118** 072017
[16] Li X, Ju L, Geng G and Jiang Q 2023 Data-driven state-of-health estimation for lithium-ion battery based on aging features *Energy* **274** 127378
[17] Xu C, Li L, Xu Y, Han X and Zheng Y 2022 A vehicle-cloud collaborative method for multi-type fault diagnosis of lithium-ion batteries *Etransportation* **12** 100172
[18] Li W, Demir I, Cao D, Jöst D, Ringbeck F, Junker M and Uwe Sauer D 2022 Data-driven systematic parameter identification of an electrochemical model for lithium-ion batteries with artificial intelligence *Energy Storage Mater.* **44** 557–70
[19] Li X, Wang Z, Zhang L, Zou C and Dorrell D D 2019 State-of-health estimation for li-ion batteries by combing the incremental capacity analysis method with grey relational analysis *J. Power Sources* **410–411** 106–14
[20] Vasta E *et al* 2023 Models for battery health assessment: a comparative evaluation *Energies* **16** 632
[21] Pastor-Fernández C, Yu T F, Widanage W D and Marco J 2019 Critical review of non-invasive diagnosis techniques for quantification of degradation modes in lithium-ion batteries *Renew. Sustain. Energy Rev.* **109** 138–59
[22] Hendricks C, Williard N, Mathew S and Pecht M 2015 A failure modes, mechanisms and effects analysis (FMMEA) of lithium-ion batteries *J. Power Sources* **297** 113–20
[23] Fu Y, Xu J, Shi M and Mei X 2022 A fast impedance calculation-based battery state-of-health estimation method *IEEE Trans. Ind. Electron.* **69** 7019–28
[24] Murariu T and Morari C 2019 Time-dependent analysis of the state-of-health for lead-acid batteries: an EIS study *J. Energy Storage* **21** 87–93
[25] Farrow V 2020 *Characterisation of Rechargeable Batteries: Addressing Fractional Ultralow-Frequency Devices* (Master of Engineering, University of Waikato)
[26] Dunn C, Scott J B, and Farrow V 2019 A multitone current sink for measuring impedance of in-use batteries *Report* (University of Waikato)
[27] Gaberšček M 2021 Understanding Li-based battery materials via electrochemical impedance spectroscopy *Nat. Commun.* **12** 6513
[28] Locorotondo E, Cultrera V, Pugi L, Berzi L, Pierini M and Lutzemberger G 2021 Development of a battery real-time state of health diagnosis based on fast impedance measurements *J. Energy Storage* **38** 102566
[29] Stroe D-I and Schaltz E 2019 Lithium-ion battery state-of-health estimation using the incremental capacity analysis technique *IEEE Trans. Ind. Appl.* **56** 678–85
[30] Peng J, Meng J, Wu J, Deng Z, Lin M, Mao S and Stroe D-I 2023 A comprehensive overview and comparison of parameter benchmark methods for lithium-ion battery application *J. Energy Storage* **71** 108197
[31] Choi W, Shin H-C, Man Kim J, Choi J-Y and Yoon W-S 2020 Modeling and applications of electrochemical impedance spectroscopy (EIS) for lithium-ion batteries *J. Electrochem. Sci. Technol.* **11** 1–13
[32] Liu C, Hu M, Jin G, Xu Y and Zhai J 2021 State of power estimation of lithium-ion battery based on fractional-order equivalent circuit model *J. Energy Storage* **41** 102954
[33] Tran M-K, Mathew M, Janhunen S, Panchal S, Raahemifar K, Fraser R and Fowler M 2021 A comprehensive equivalent circuit model for lithium-ion batteries, incorporating the effects of state of health, state of charge and temperature on model parameters *J. Energy Storage* **43** 103252
[34] Tran M-K, DaCosta A, Mevawalla A, Panchal S and Fowler M 2021 Comparative study of equivalent circuit models performance in four common lithium-ion batteries: LFP, NMC, LMO, NCA *Batteries* **7** 51
[35] Farrow V, Scott J, Cree M J and Wilson M 2024 Passive, fractional, battery equivalent-circuit model in time and frequency domains part 1: linear model *IEEE Access* **12** 64589–98
[36] Wilson M T, Dunn C J, Farrow V, Cree M J and Scott J B 2024 Efficiency of cycled batteries analyzed through voltage-current phase differences *IEEE Access* **12** 36202–11

[37] Wang X, Wei X, Chen Q and Dai H 2021 A novel system for measuring alternating current impedance spectra of series-connected lithium-ion batteries with a high-power dual active bridge converter and distributed sampling units *IEEE Trans. Ind. Electron.* **68** 7380–90
[38] Dunn C J 2024 Characterisation and prediction of state of health of rechargeable batteries *PhD Thesis* University of Waikato, Hamilton, New Zealand
[39] Dunn C and Scott J 2022 Achieving reliable and repeatable electrochemical impedance spectroscopy of rechargeable batteries at extra-low frequencies *IEEE Trans. Instrum. Meas.* **71** 1–8
[40] Lu X, Li H and Chen N 2019 An indicator for the electrode aging of lithium-ion batteries using a fractional variable order model *Electrochim. Acta* **299** 378–87
[41] Levenberg K 1944 A method for the solution of certain problems in least squares *Q. Appl. Math.* **2** 164–8
[42] Marquardt D 1963 An algorithm for least-squares estimation of nonlinear parameters *SIAM J. Appl. Math.* **11** 431–41
[43] Ortigueira M D 2024 Principles of fractional signal processing *Digit. Signal Process.* **149** 104490
[44] Ortigueira M D and Machado J T 2022 The 21st century systems: an updated vision of continuous-time fractional models *IEEE Circuits Syst. Mag.* **22** 36–56
[45] Sabatier J, Aoun M, Oustaloup A, Grégoire G, Ragot F and Roy P 2006 Fractional system identification for lead acid battery state of charge estimation *Signal Process.* **86** 2645–57
[46] Teodoro G S, Machado J A T and de Oliveira E C 2019 A review of definitions of fractional derivatives and other operators *J. Comput. Phys.* **388** 195–208
[47] Zou C, Zhang L, Hu X, Wang Z, Wik T and Pecht M 2018 A review of fractional-order techniques applied to lithium-ion batteries, lead-acid batteries and supercapacitors *J. Power Sources* **390** 286–96
[48] Ortigueira M D 2022 A new look at the initial condition problem *Mathematics* **10** 1771
[49] Kaiser G 2011 *A Friendly Guide to Wavelets* (Birkhäuser)
[50] Clemson P, Lancaster G and Stefanovska A 2016 Reconstructing time-dependent dynamics *Proc. IEEE* **104** 223–41
[51] Clemson P and Stefanovska A 2014 Discerning non-autonomous dynamics *Phys. Rep.* **542** 297–368
[52] Du R, Wang X, Dai H, Wei X and Ming P 2021 Online impedance spectrum measurement of fuel cells based on Morlet wavelet transform *Int. J. Hydrog. Energy* **46** 24339–52
[53] Hoshi Y, Yakabe N, Isobe K, Saito T, Shitanda I and Itagaki M 2016 Wavelet transformation to determine impedance spectra of lithium-ion rechargeable battery *J. Power Sources* **315** 351–8
[54] El-Dalahmeh M'd, Al-Greer M, El-Dalahmeh M'ath and Bashir I 2023 Capacity estimation of lithium-ion batteries based on adaptive empirical wavelet transform and long short-term memory neural network *J. Energy Storage* **70** 108046
[55] Zhang Z-L, Cheng X, Lu Z-Y and Gu D-J 2016 SOC estimation of lithium-ion batteries with AEKF and wavelet transform matrix *IEEE Trans. Power Electron.* **32** 7626–34
[56] Xu J, Mei X, Wang X, Fu Y, Zhao Y and Wang J 2020 A relative state of health estimation method based on wavelet analysis for lithium-ion battery cells *IEEE Trans. Ind. Electron.* **68** 6973–81
[57] Iatsenko D, McClintock P V E and Stefanovska A 2015 Linear and synchrosqueezed time-frequency representations revisited: Overview, standards of use, resolution, reconstruction, concentration and algorithms *Digit. Signal Process.* **42** 1–26
[58] Barnes S J K, Bjerkan J, Clemson P T, Newman J and Stefanovska A 2024 Phase coherence-a time-localized approach to studying interactions *Chaos* **34** 073155
[59] Bandrivskyy A, Bernjak A, McClintock P and Stefanovska A 2004 Wavelet phase coherence analysis: application to skin temperature and blood flow *Cardiovascular Eng. Int. J.* **4** 89–93
[60] Lachaux J-P, Rodriguez E, Le Van Quyen M, Lutz A, Martinerie J and Varela F J 2000 Studying single-trials of phase synchronous activity in the brain *Int. J. Bifurcation Chaos* **10** 2429–39
[61] Wilson M T, Dunn C, Farrow V, Mucalo M and Scott J B 2023 Measuring electrical properties of batteries at ultra-long timescales *NCSLI Meas. J. Meas. Sci.* **15** 12–16
[62] Sheppard L W, Stefanovska A and McClintock P V E 2012 Testing for time-localized coherence in bivariate data *Phys. Rev.* E **85** 046205
[63] Lancaster G, Iatsenko D, Pidde A, Ticcinelli V and Stefanovska A 2018 Surrogate data for hypothesis testing of physical systems *Phys. Rep.* **748** 1–60
[64] Ortigueira M D, Martynyuk V, Kosenkov V and Guimarães Batista A 2023 A new look at the capacitor theory *Fractal Fract.* **7** 86
[65] Hartley T T, Trigeassou J-C, Lorenzo C F and Maamri N 2015 Energy storage and loss in fractional-order systems *J. Comput. Nonlinear Dyn.* **10** 061006
[66] Sabatier J 2020 Beyond the particular case of circuits with geometrically distributed components for approximation of fractional order models: application to a new class of model for power law type long memory behaviour modelling *J. Adv. Res.* **25** 243–55
[67] Holm S, Holm T and Martinsen Ørjan G 2021 Simple circuit equivalents for the constant phase element *PLoS One* **16** e0248786
[68] Kabir M M and Emre Demirocak D 2017 Degradation mechanisms in li-ion batteries: a state-of-the-art review *Int. J. Energy Res.* **41** 1963–86
[69] Wilson M T, Cowie L, Farrow V, Cree M J and Scott J B 2024 Rapid time-domain simulation of fractional capacitors with SPICE *J. Comput. Electron.* **23** 677–89
[70] Moskon J, Jamnik J and Gaberscek M 2013 In depth discussion of selected phenomena associated with intrinsic battery hysteresis: battery electrode versus rubber balloons *Solid State Ion.* **238** 24–29
[71] Newman Julian, Lancaster Gemma and Stefanovska Aneta Lancaster University Physics 2018 *MODA* https://github.com/luphysics/MODA
[72] Wilson Marcus T 2024 *Fractional ECM Fitting* https://github.com/mtwilson1970/Fractional_ECM_fitting